



Cite this: DOI: 10.1039/c4cp04264f

Structural disordering of de-alloyed Pt bimetallic nanocatalysts: the effect on oxygen reduction reaction activity and stability†

Ioannis Spanos,^{*a} Knud Dideriksen,^a Jacob J. K. Kirkensgaard,^b Stanislav Jelavic^a and Matthias Arenz^{*a}

Platinum bimetallic alloys are well-known for their ability to catalyze the oxygen reduction reaction (ORR) in proton exchange membrane fuel cells (PEMFCs). Pt_xCo_{1-x} colloidal nanoparticles were synthesized with varying initial Pt:Co ratios, but constant size to investigate how the initial metal composition affects their electrocatalytic performance. The results show that upon contact with acid environment the Co leaches out of the particles leading to almost identical compositions, independent of the initial differences. Surprisingly the data show a clear trend in ORR activity, although the Pt_xCo_{1-x} nanoparticles almost completely de-alloy during acid leaching, *i.e.* under reaction conditions in a fuel cell. To scrutinize the resulting particle structure after de-alloying we used pair distribution function (PDF) analysis and X-ray diffraction (XRD) gaining insight into the structural disorder and its dependence on the initial metal composition. Our results suggest that not only the ORR activity, but also the corrosion resistance of the synthesized NPs, are dependent on the structural disorder resulting from the de-alloying process.

Received 22nd September 2014,
Accepted 15th December 2014

DOI: 10.1039/c4cp04264f

www.rsc.org/pccp

1. Introduction

Burning hydrocarbon based fuels for energy conversion is thermodynamically unfavorable and environmentally unfriendly. With the development of fuel cells, renewable fuels like hydrogen have started to become attractive in the fuel market, especially in the automotive industry. Proton exchange membrane fuel cells (PEMFCs) offer thermodynamic conversion efficiency of up to 85%, in comparison to the thermodynamic conversion efficiency of ~35% of internal combustion engines. Additionally, in the case of using hydrogen generated by electrolysis as fuel, the only by-products produced are heat and water.¹ However, a disadvantage of PEMFCs is their cost and the amount of required Pt catalyst; the latter being a limiting factor for their wide use. In other words, for PEMFCs to become competitive in the automotive market, the amount of platinum used needs to be significantly reduced. As a rough estimate, for using the same amount of precious metal in a fuel cell car as is nowadays used in the automotive converter of conventional cars, a reduction in Pt content by a factor of 10 is necessary.

Several research groups therefore try to develop fuel cells using no precious metals at all. Although significant advances have been made in recent years concerning the catalytic activity of such non-precious metal catalysts, their low stability^{2,3} and relative poor performance at very high current densities call for further advances before being a viable alternative to Pt based catalysts. As a consequence Pt based catalysts will be the first to be commercialized in fuel cell cars⁴ and tremendous focus lies on improving these precious metal catalysts. One frequently discussed option for doing so is using Pt alloys instead of pure Pt in the catalyst. Not only is the specific and mass activity for the oxygen reduction reaction enhanced on Pt alloys as compared to pure platinum, but their cost is also reduced as some Pt is replaced by non-noble metals like Ni, Co, Fe, Cu *etc.*⁵⁻⁸ The drawback, however, is that Pt-alloys are not stable in acid environment and the non-noble component leaches out.⁹ As a consequence, the effective performance of such catalyst in real fuel cells can be significantly worse than the one of pure Pt catalyst¹⁰ and an acid washing treatment is necessary before their use in a fuel cell. In the following, we will refer to such samples as de-alloyed catalysts.

In the presented work we investigate how alloying – and subsequent de-alloying – of Pt with different amounts of Co effects the structure, activity and stability of such fuel cell catalysts. In order to study these effects systematically, a proper method for the catalyst preparation is crucial. The most common method used for catalyst preparation is based on impregnation/precipitation.

^a Nano-science Center, Department of Chemistry, University of Copenhagen, Universitetsparken 5, DK-2100 Copenhagen Ø, Denmark.

E-mail: ioaspanos@chem.ku.dk, m.arenz@chem.ku.dk

^b Niels Bohr Institute, University of Copenhagen, Universitetsparken 5, DK-2100, Copenhagen Ø, Denmark

† Electronic supplementary information (ESI) available. See DOI: 10.1039/c4cp04264f

Such catalysts can exhibit excellent oxygen reduction reaction (ORR) activity.¹¹ However, the control over the synthesis is often limited and the particle size at maximum activity is relatively large.^{12,13} The limited control of the synthesis is a consequence of the fact that the reduction of the metal precursors is a slow process when using excess solvent and thus the reduction rate is usually enhanced with the help of a reducing agent (*e.g.* NaBH₄). Furthermore, the as prepared catalysts are usually heat treated to decompose any remaining organics and to enhance alloying. Thus usually the resulting particle size distribution is wide and such catalysts are difficult to use for studying the de-alloying as a function of particle composition. Furthermore, large particles may exhibit the highest mass activity, however, at high current densities their performance is also prone to diffusion problems of the reactant.

Alternatively, a colloidal approach can be used for the particle synthesis. In such a synthesis the Pt or Pt-alloy NPs the catalysts are prepared in two separate steps.^{14–16} First a colloidal solution of Pt or Pt alloy NPs is prepared using a simple reflux method in a mild reducing environment using ethylene glycol or other polyols as reducing agents, usually in the presence of a capping agent. Afterwards the prepared unsupported colloidal NPs are washed to separate the NPs from the solvent and then dispersed on a high surface area (HSA) support like carbon black. Further post heat treatment may be employed, although in our case we avoided such treatment, thus preparing NPs of uniform size distributions.

The method used in this work is based on a modified colloidal synthesis route for the preparation of Pt catalysts, which has been shown to be ideally suited for systematic studies.^{17,18} As compared to the preparation of pure Pt NPs, here we use specific ligands as capping agents, *i.e.* hexadecyl trimethyl ammonium bromide (CTAB), which promotes the mixing between platinum and cobalt in a controlled way. Employing acid washing, we can remove any residual organics from the NPs surface and de-alloy the initially well-defined Pt_xCo_{1-x} NPs. We avoid any heat treatment of the NPs, although this has been shown to induce Pt segregation to the surface and the formation of Pt (shell)–Co (core) structures, which have been reported to exhibit a remarkable strain induced activity increase.¹⁹ The reasoning not to apply any heat treatment was that it would have considerably influenced the catalysts and would have made the different catalysts less comparable. However, we try to observe trends, not necessarily to prepare the best catalyst. Upon heat treatment not only the particle size increases in a difficult to control manner due to sintering. Also the structure of the materials, *i.e.* nanoparticles and support may change as function of composition.

2. Experimental details

2.1 Catalyst synthesis

The investigated catalysts, hereafter denoted as Pt_xCo_{1-x}/C, were synthesized using a modification of a recently developed colloidal synthesis approach. The synthesis consists of two steps.

First, a solution of colloidal NPs with narrow size distribution is prepared in ethylene glycol (EG), and then the NPs are deposited onto the HSA carbon support. In detail, the colloidal suspension of the Pt-alloy NPs is synthesized according to the following recipe. For the Pt₃Co NP samples, a 1 ml solution of EG containing 19.3 mg of H₂PtCl₆·6H₂O and 2.96 mg of CoCl₂·6H₂O precursors was added drop wise to a 1 ml EG solution containing 0.4 M NaOH in room temperature. After stirring for 15 minutes the temperature of the solution was raised to 165 °C using a microwave assisted synthesis system (Discover and Explorer SP by CEM equipped with a camera) and kept at this temperature for 5 min. At around 110 °C the solution turned black indicating the formation of NPs. For the preparation of PtCo, PtCo₃ and PtCo₆ NPs the synthesis procedure was similar, but with different Pt and Co precursor amounts. In all cases the total metal concentration in the EG was kept to 4 g l⁻¹.

As this synthesis showed limited control over the effective particle composition, in addition we prepared catalysts by adding CTAB as capping agent to the EG. We applied an amount equal to 3 times of the total metal moles mixed together with 1 ml of the Pt and Co precursors in EG solution. As shown, the above procedure improves the co-reduction and mixing of Pt and Co and thus the stoichiometric composition of the NPs. To investigate the effect of CTAB on the structural properties of the nanoalloys, selected samples were prepared for structural characterization only with lower molar ratios of CTAB:total metal of 0, 1 and 2. These will be marked with a superscript denoting the ratio (*e.g.*, PtCo⁰ for PtCo prepared without CTAB).

After synthesis, the NP solutions are stable over prolonged time. Before use as catalysts, the NPs were deposited onto Ketjenblack EC-300 (AkzoNobel, Brunauer–Emmett–Teller (BET) surface area: 795 m² g⁻¹) by washing specific amounts of Pt alloy colloidal solutions in HCl to obtain samples with 40 wt% Pt loading on the carbon support. The washed NPs were centrifuged for 10 min at 4000 rpm. The supernatant solution was discarded and the procedure was repeated until the supernatant was clear, which indicates that ethylene glycol residues were removed. Finally, sonication of the NPs together with the carbon support in acetone promoted the distribution of the NPs on the support yielding catalysts with high surface area (see Fig. 1).

2.2 Physical characterization

The electrocatalysts were characterized by transmission electron microscopy (TEM) using a Tecnai T20 G2 (Philips FEI, Oregon, USA) equipped with a thermionic electron gun operated at 200 kV. The nanoparticle composition, *i.e.* the Pt:Co ratio and Pt loading, were determined by energy dispersive X-ray spectrometry (EDS) in the TEM and confirmed with inductively coupled plasma (ICP) measurements and energy dispersive X-ray spectroscopy in a scanning electron microscope (SEM). For the ICP measurements the NPs were completely dissolved in aqua regia. SEM EDS was applied to evaluate the bulk metal composition of the nanocatalysts, compared to the results in TEM. To determine the initial Pt:Co ratio, the NPs were washed with isopropanol instead of HCl, which is expected to have no

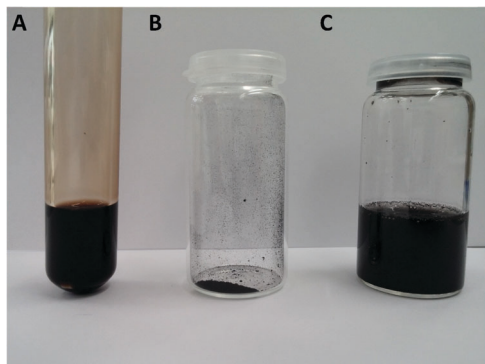


Fig. 1 (A) Pt-alloy nanoparticles in colloidal solution, (B) HCl washed Pt-alloy nanoparticles dispersed on HSA carbon powder. (C) Fuel cell catalysts ink of 40% wt Pt on carbon.

effect on the NP composition. The platinum particle size distribution of the supported catalysts was further determined by X-ray scattering using a SAXS/SLAB instrument (JJ-Xray, Denmark) equipped with a Rigaku 100XL+ micro focus sealed X-ray tube and a Dectris 2D 300K Pilatus detector. On this instrument, the detector is moveable allowing different q -ranges to be accessed for the measurement of both Small-Angle and Wide-Angle X-ray Scattering (SAXS/WAXS). Here the magnitude of the scattering vector is defined as $q = 4\pi/\lambda\sin(\theta)$ with λ being the X-ray wavelength and θ half of the scattering angle. Samples were sealed between two 5–7 μm thick mica windows and measurements were performed *in vacuo*.

To elucidate the particle structure, high-energy X-ray scattering was conducted at beamline 11-ID-B at the Advanced Photon Source using an X-ray wavelength of 0.2127 Å. The scattered X-rays were detected by a ~ 40 cm by ~ 40 cm amorphous Si 2D detector (Perkin Elmer) at a distance of ~ 16 cm from the sample. Using a CeO_2 standard, the scattering geometry was calibrated with Fit-2D.^{20,21} This software was also used for converting two-dimensional data to polarization corrected one-dimensional data, from which pair distribution functions (PDFs) were obtained with PDFGETX2.^{22,23} Data treatment in PDFGETX2 included standard corrections, such as subtraction of background (capillary tubes with the carbon substrate), subtraction of incoherent scattering, normalization by the sample's average atomic scattering cross section and corrections for non-linear detector efficiency. In the treatment, all samples were assumed to bear only Pt. PDFs were acquired from Fourier transform of the reduced scattering structure function, $F(Q)$, using a maximum Q of 22.3 \AA^{-1} . Real space fitting of PDFs was carried out with PDFgui²⁴ and structural data for Pt,²⁵ using an instrumental dampening of 0.037 (Q_{damp}) and broadening of 0.017 (Q_{broad}) refined from PDFs of natural quartz. Ignoring other effects on peak width, this instrumental broadening would be expected to result in peak widths being 3% larger at $r = 15 \text{ \AA}$. The following parameters were fitted simultaneously: (1) Scaling, size of coherently scattering domains (assumed spherical) and correlated atomic movement (d_2), (2) lattice constant parameter, and (3) an atomic isotropic displacement parameter, U_{iso} . The PDFs were fitted in the r -range 2.4–40 Å to encompass all peaks.

Finally, powder diffraction patterns were collected with Bruker D8 Advance X-ray diffractometer in a Bragg–Brentano geometry using $\text{Co-K}\alpha$ radiation with Fe-filter and LynxEye detector with opening angle of 2.712° . Soller slits at incident and diffracted beam were set to 2.5° , divergence slit to 0.3° and antiscatter slit to 3° . The pattern was collected from 30 until $120^\circ 2\theta$ with $0.04^\circ 2\theta$ step size and 12 seconds per step in a continuous mode. Sample was dispersed in ethanol and slurry was dropped on a zero background silicon plates, it was let to dry and spun at 20 rpm during the analysis. All patterns were collected at room temperature under ambient conditions.

2.3 Electrochemical characterization

The electrochemical characterization of the catalysts was conducted in a three-electrode electrochemical cell with a glassy carbon (GC) rotating disk electrode (RDE, Radiometer analytical, France) 5 mm in diameter, as a working electrode (WE). A Pt mesh was used as a counter electrode (CE) for the activity measurements whereas for the stability measurements a carbon rod was used to avoid corrosion of the Pt mesh electrode and concomitant Pt re-deposition on the working electrode. A saturated calomel electrode (SCE) was used as reference electrode (RE), but all potentials are given with respect to the reversible hydrogen electrode (RHE) potential, which was experimentally determined before each measurement series. A home-built potentiostat was used for the measurements.²⁶

In order to obtain a thin catalyst film on the GC WE the catalyst powders were mixed with Millipore water and a known quantity of catalyst ink was pipetted onto the GC electrode to obtain a Pt loading of $14 \mu\text{g}_{\text{Pt}} \text{ cm}^{-2}$. Thereafter the ink was left to dry on the GC electrode under a N_2 stream. As in our previous work, no Nafion binder was used for the catalyst ink to adhere on the GC electrode. During the electrochemical measurements, the WE potential was compensated for the IR drop to obtain a residual resistance of less than 3 Ohm.

The ORR activity was determined in 0.1 M HClO_4 prepared from Millipore[®] water ($> 18.3 \text{ M}\Omega \text{ cm}$, $\text{TOC} < 5 \text{ ppb}$) and HClO_4 (Merck suprapur). The measurements were performed at room temperature. Prior to the measurements the electrolyte was de-aerated by purging with Ar gas (99.998%, Air Liquide), and the measurements were started with cleaning the catalyst by potential cycles between 0.05 and 1.1 V_{RHE} at a scan rate of 50 mV s^{-1} . The specific activity of the ORR was determined in accordance to our previous work from the positive going RDE polarization curves recorded in O_2 saturated electrolyte at a scan rate of 50 mV s^{-1} and a rotation speed of 1600 rpm. The polarization curves were corrected for the non-faradaic background by subtracting the CVs recorded in Ar-purged electrolyte.²⁷ The electrochemical surface area (ECSA) of the catalysts was determined from the CO stripping charge recorded at a sweep rate of 50 mV s^{-1} . Mass activities of the prepared catalysts were determined after correcting the nominal Pt loading by the one determined in the ICP measurements, *i.e.* usually nominal and actual Pt loading deviate by *ca.* 20%.

2.4 Accelerated stress test protocol (AST)

The degradation treatment of the catalysts was employed in a multi working electrode setup (MWE). A stress test protocol by FCCJ,

simulating load-cycle condition, consisting of square wave cycles from 0.6 to 1.0 V_{RHE} keeping the potential constant at each value for three seconds, was used to test the stability properties of the Pt-alloy nanocatalysts. The total treatment lasted 9000 cycles (15 hours), during which the ECSA drop was regularly monitored by CO stripping measurements. All the measurements were conducted in room temperature, without rotation.

3. Results/discussion

To de-alloy the NPs, a simple washing technique with a 1 M HCl solution was used. The great advantage of this technique is that any residual ethylene glycol and CTAB on the NP surface, which are known to reduce the catalytic performance,^{15,28} are removed (see sketch in Fig. 2) without inducing particle agglomeration. EDS measurements show that the NP synthesis with addition of CTAB has a significant effect on the initial amount of Co present in the NPs (see Table 1 and Fig. S1, ESI[†]). The Pt:Co ratio of the NPs synthesized with CTAB is close to the theoretically expected one, whereas in synthesis without CTAB the amount of Co is significantly lower than the one expected, indicating that CTAB enhances the mixing of Pt and Co. From the XRD data, we have no evidence to assume that the pristine samples contain both $\text{Pt}_x\text{Co}_{1-x}$ NPs together with pure Co NPs (and pure Pt NPs). Further, in literature it is reported that no pure Co NPs can be prepared using the polyol method, unless surfactants like polyvinyl pyrrolidone (PVP) or CTAB are used.^{29–31} In these cases, the obtained Co NPs exhibit significantly larger sizes as observed in our work. Here we never observed NPs larger than 4 nm and thus we assume that Pt and Co form mixed particles as illustrated in Fig. 2.

Washing in HCl not only removes EG and CTAB from the surface of the NPs, but also leaches out Co. Compositional analysis shows that independent of the initial Co content only a small amount of Co ($\sim 5\%$) was left intact in the core of the NPs after the acid washing (see Table 1), *i.e.* within the experimental accuracy the composition of the different de-alloyed catalysts is identical.

Table 1 Summary of Pt alloy properties. The initial metal content of alloys, both synthesized with and without the presence of CTAB, has been acquired after an isopropanol washing step which we expect to have no effect on the Co content

Pt alloys	Pt:Co initial content	Pt:Co CTAB initial content	Pt:Co CTAB content after acid-leaching
Pt	—	—	—
Pt ₃ Co	86:14	72:28	95:5
PtCo	70:30	56:44	92:8
PtCo ₃	52:48	29:71	93:7
PtCo ₆	40:60	13:87	96:4

In the following, we will only discuss the acid-leached catalysts prepared using CTAB if not specifically noted otherwise. TEM and SAXS analysis of the acid-leached samples are shown in Fig. 3. Both methods reveal size distributions with an average particle size around 2 nm. In agreement with previous results³² the size distribution from SAXS is slightly shifted to smaller sizes as compared to the size histogram obtained from TEM. More importantly, both methods indicate that the particle size of the catalysts increases with increasing initial amount of Co even though the final Co composition is $\sim 5\%$ in all catalysts. An exemption is the particle size of PtCo₆, which is significantly decreased as compared to PtCo₃. Its particle size is close to the one of pure Pt NPs, suggesting that extensive de-alloying leads to a structural collapse of the PtCo₆ particles. However, due to the small size of the NPs, a direct observation of such a particle collapse is not observable from the microscopic measurements.

The electrochemical properties and ORR performance of the different de-alloyed samples were studied in half-cell RDE measurements. In Fig. 4 cyclic voltammograms, representative ORR polarization curves, and corresponding Tafel plots are displayed. All characteristic properties of the catalysts as well as their surface areas calculated from CO stripping are summarized in Table 2. The cyclic voltammograms were recorded in argon saturated 0.1 M HClO₄ solutions, the polarization curves in the same electrolyte, but saturated with oxygen. The cyclic voltammograms show the typical features of Pt-based catalysts with a H_{upd} region, a double layer region and a potential region of oxide formation.^{33–35} No large differences in the CVs of the

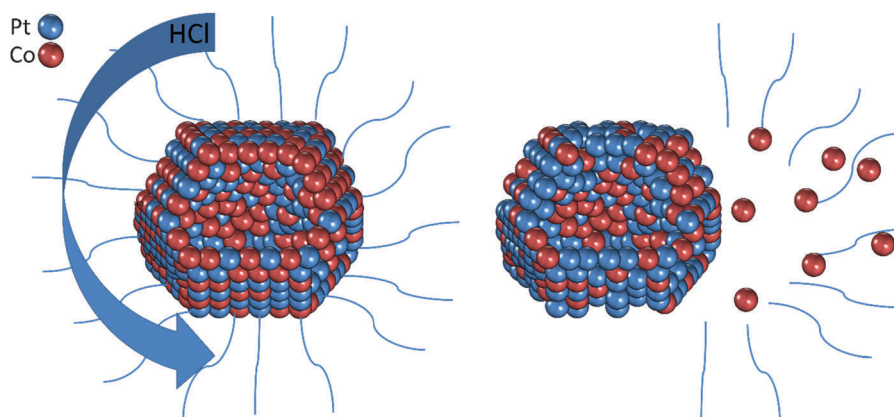


Fig. 2 Acid washing treatment with 1 M HCl de-alloys $\text{Pt}_x\text{Co}_{1-x}$ nanoalloys and removes any residual EG and CTAB.

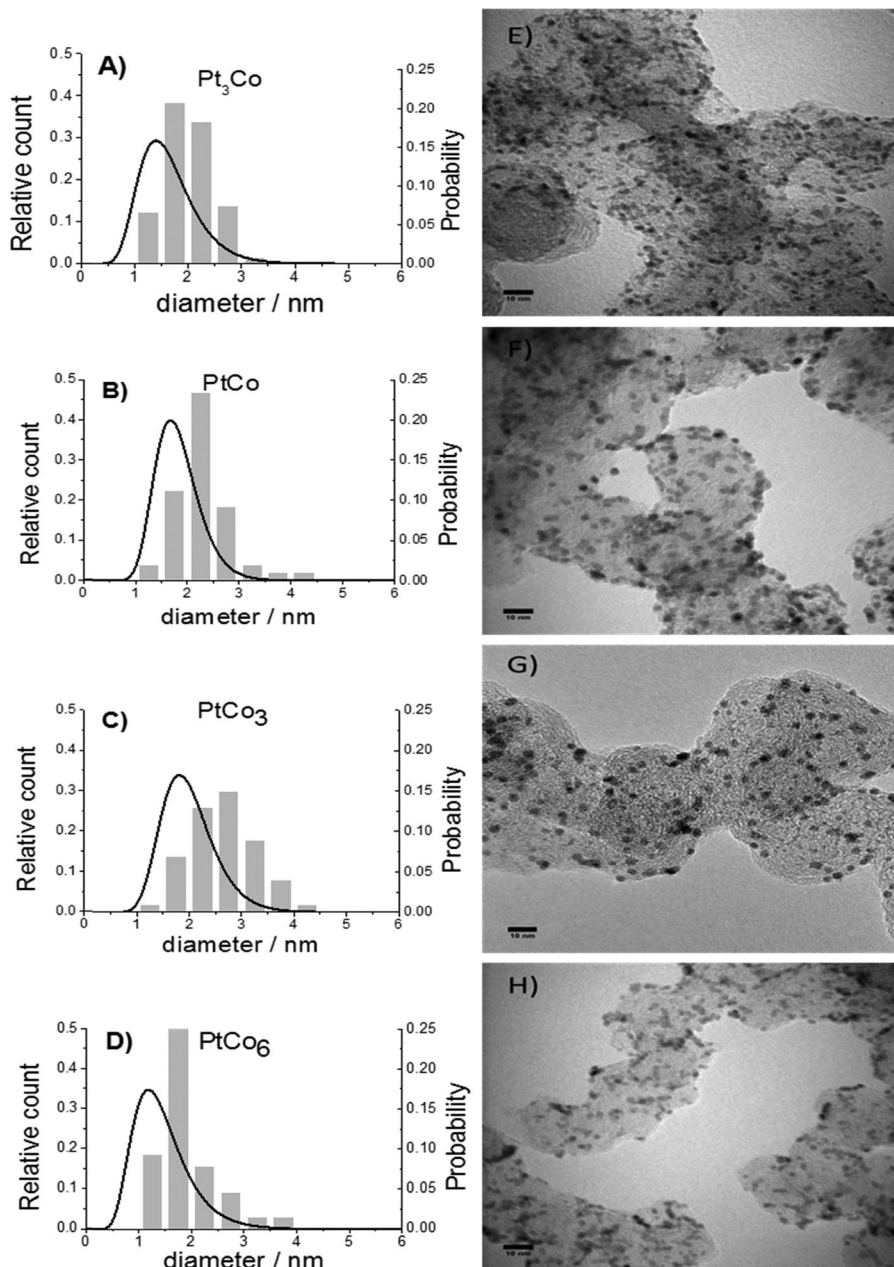


Fig. 3 Particle size distributions of de-alloyed CTAB synthesized $\text{Pt}_x\text{Co}_{1-x}/\text{C}$ catalysts established from TEM (histograms/left scale) and SAXS (black line/right scale). Estimated average values of nanoparticle size (diameter) are: Pt (~ 1.8 nm), Pt_3Co (~ 2 nm), PtCo (~ 2.3 nm), PtCo_3 (~ 2.6 nm) and PtCo_6 (~ 1.9 nm).

catalysts are observed, however, the H_{upd} region reflects the different surface areas.

Furthermore some small trends may be identified in the region of OH (or oxide) formation and its reduction (see Fig. S2, ESI[†]). The onset potentials of OH_{ad} (or oxide) formation and reduction shift slightly towards lower values with increasing initial Co content, until the critical PtCo_6 composition, where both potentials shift towards higher values. This finding is in contrast to what is usually observed, meaning that a negative shift of the aforementioned potentials is typically ascribed to a lower catalytic activity. However, both specific and mass specific activities follow the order $\text{Pt} < \text{PtCo}_6 < \text{Pt}_3\text{Co} < \text{PtCo} < \text{PtCo}_3$,

indicating that cyclic voltammetry, being an averaging method, reflects the total number of surface sites and not specifically the catalytic sites responsible for the observed trend in ORR performance.

Probing the ORR activity on the different samples, the polarization curves exhibit a region of well-defined diffusion-limited current at lower potentials, a mixed kinetic-diffusion controlled potential region suitable for extraction the ORR activity around 0.9 to 0.975 V_{RHE} . Furthermore, all curves terminate at zero current at potentials larger than 1 V_{RHE} .

The respective Tafel plots of the catalysts reveal a clear catalytic performance enhancement with increasing initial cobalt content.

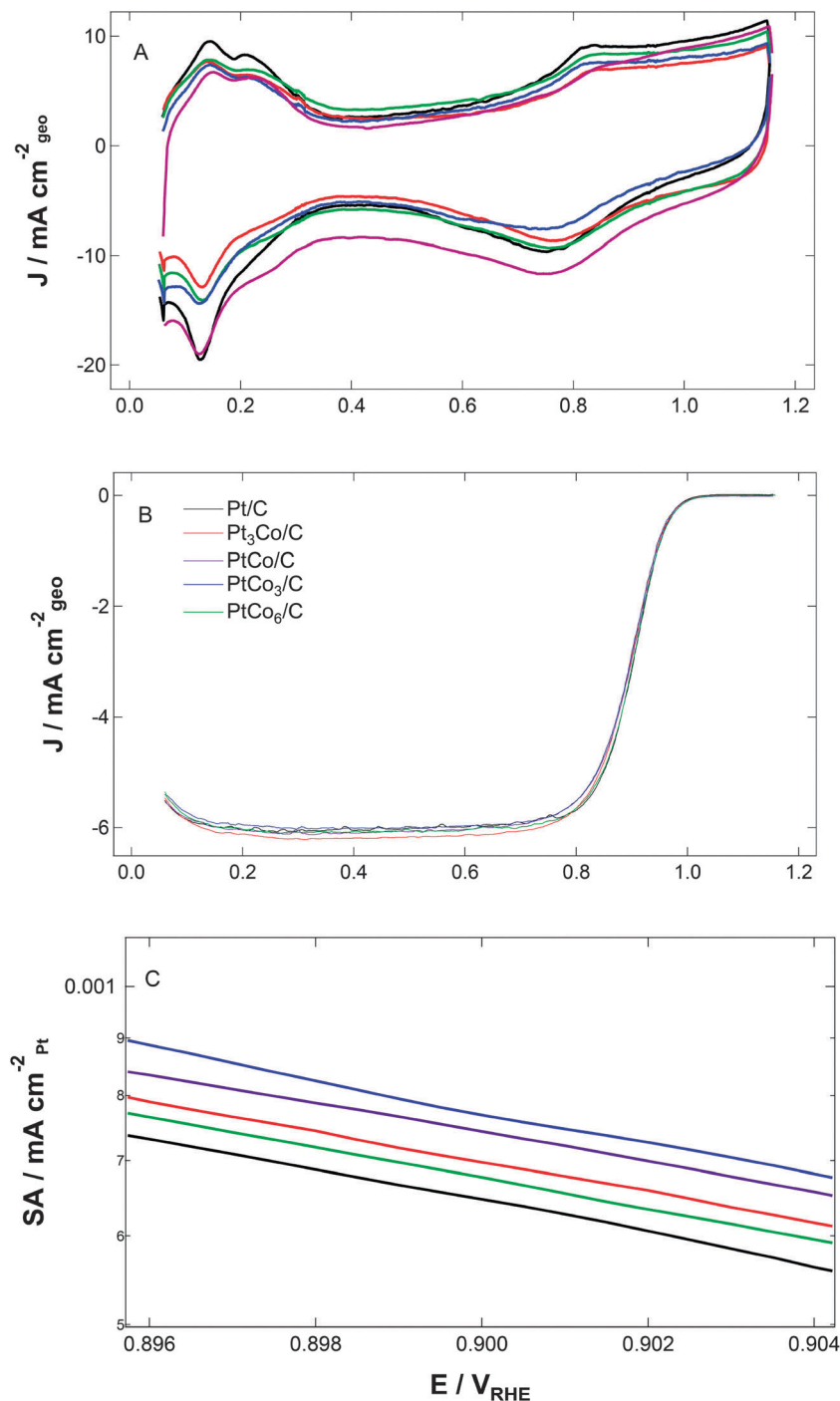


Fig. 4 (A) Cyclic voltammograms recorded at a 50 mV s^{-1} scan rate, in a 0.1 M HClO_4 Ar-saturated solution, (B) positive going ORR curves and (C) respective Tafel plots of the specific activity, of $\text{Pt}_x\text{Co}_{1-x}/\text{C}$ catalysts recorded at a 50 mV s^{-1} scan rate, in a 0.1 M HClO_4 O_2 -saturated solution. A rotation speed of 1600 rpm was chosen.

The specific and mass activities of PtCo_3/C are more than 50% increased as compared to Pt/C , which was prepared by the same colloidal approach and serves as benchmark. The activity of the PtCo_6/C sample, which showed signs of structural collapse, however, is decreased and similar to the Pt/C benchmark. To illustrate the observed trends in specific and mass activity for the ORR, they are displayed once more in Fig. 5.

The main purpose of this study is to show trends in catalytic performance in samples that are prepared under comparable conditions. Nevertheless and although the improvement factor is relatively low in comparison with previous work reported in the literature where the samples have been heat treated, it is still significant. The advantage of the catalysts reported here, however, is their high ECSA, which is beneficial at high current

Table 2 Specific and mass activities of the CTAB synthesized de-alloyed $\text{Pt}_x\text{Co}_{1-x}/\text{C}$ samples determined in ORR polarization measurements in 0.1 M HClO_4 at 50 mV s^{-1} . The ECSA determination was corrected for the Pt content determined in ICP measurements

Pt alloys	Specific activity ($\text{mA cm}_{\text{Pt}}^{-2}$)	Mass activity ($\text{mA mg}_{\text{Pt}}^{-1}$)	ECSA ($\text{m}^2 \text{g}^{-1}$)
Pt/C	0.531	494	93
$\text{Pt}_3\text{Co}/\text{C}$	0.682	580	85
PtCo/C	0.774	619	80
PtCo_3/C	0.883	662	75
PtCo_6/C	0.621	546	88

densities in a PEMFC. Maybe even more important, the catalysts are already almost completely de-alloyed and will not lead to a poisoning of the Nafion membrane during de-alloying under operation.

In addition to the catalytic performance, we tested the degradation resistance of the catalysts in accelerated stress tests (ASTs). We choose a test protocol from the FCCJ that simulates load-cycle conditions of fuel cells under operation. Under load cycle conditions the stability of the catalysts depends on the degradation resistance of the active phase, *i.e.* the catalyst particles. The main degradation channels under such conditions are Pt dissolution and particle migration and coalescence. By comparison simulating start up/shut down conditions the degradation mainly depends on the HSA support.³⁶

Thus in this work we investigate how the structural properties of the $\text{Pt}_x\text{Co}_{1-x}$ alloy nanoparticles affect Pt dissolution as well as particle migration and coalescence. As seen in Fig. 6, a clear trend in degradation resistance with the initial Co content is observed. The degradation resistance of the catalysts increases with the degree of Pt and Co mixing in the initial, as prepared, samples. As seen in Fig. 6 for the case of Pt/C, typically the ECSA loss during the initial treatment, *i.e.* the first *ca.* 2000 cycles, is highest; thereafter the degradation rate per cycle is reduced and the degradation curve somehow flattens out. The de-alloyed $\text{Pt}_x\text{Co}_{1-x}$ nanoparticles exhibit an improved degradation resistance in these first 2000 cycles. Thereafter the degradation rate, *i.e.* the degradation per cycle, is very similar for all samples. One sample, however, exhibits different behavior. In the case of the PtCo_6/C sample the ECSA loss during the first 1000 cycles is the highest compared to the rest of the samples, *i.e.* the cause for the initial degradation is

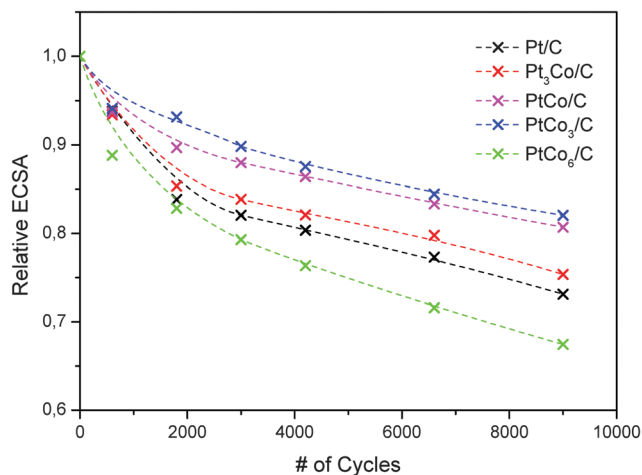


Fig. 6 Degradation behavior of the supported nanocatalysts under simulated load-cycle AST protocol from the FCCJ. The measurements were conducted in Ar saturated 0.1 M HClO_4 electrolyte without rotation. The relative ECSA is plotted as a function of the number of cycles. Crosses indicate the cycle number at which ECSA was determined. Dashed-line fittings serve only as a guide for the reader.

greatly enhanced. Furthermore, after the first 1000 cycles the degradation rate of PtCo_6/C remains high over an extended period of potential. This indicates that the structural integrity of the excessively de-alloyed particles is completely lost. Evidence for the reason of the different stability may be obtained from the characteristic CO stripping plots and cyclic voltammograms recorded during the AST treatment (see Fig. S3, ESI[†]). While for Pt/C the peak potential of the CO stripping peak shifts to higher potentials after degradation, indicating particle growth, the shift of the peak potential of the CO stripping peak of the PtCo_3/C , is minimal. The same is true for the cyclic voltammograms recorded in Ar saturated solution. While for Pt/C the characteristic shift of OH_{ad} formation and reduction is observed upon continuous AST treatment, the voltammogram of the PtCo_3/C sample stays relative unaffected, except for the loss in ECSA. Even though more work is necessary to analyze this finding, it can be stated that de-alloying positively influences the stability of NPs, however, if excessive structural changes are inflicted (as for PtCo_6) the NPs become unstable.

Having disclosed the trends in ORR activity and stability of $\text{Pt}_x\text{Co}_{1-x}/\text{C}$ catalysts, we carefully characterized their structure.

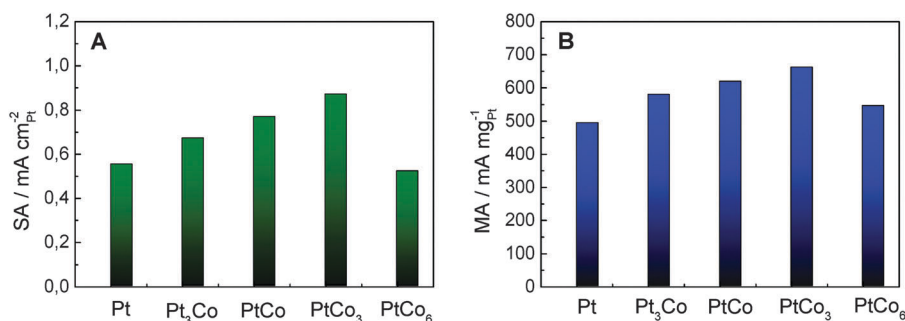


Fig. 5 (A) Specific and (B) mass activities of $\text{Pt}_x\text{Co}_{1-x}/\text{C}$ catalysts, synthesized with the addition of CTAB and de-alloyed, depicting the effect of the degree of alloying and subsequent de-alloying on the catalytic performance.

A common analysis tool is XRD to determine deviations of the lattice constant of the bare metal. We characterized both the pristine and de-alloyed samples. XRD measurements of the pristine samples are less defined as organic impurities present on the samples lead to wider diffraction peaks, as compared to the de-alloyed samples. Nevertheless, with increasing initial Co content a shift of the Pt(111) diffraction peak towards higher angles was observed in both cases indicating lattice constraint and a change in the interatomic distance of Pt (see Fig. S4, ESI†). In the case of the de-alloyed samples this shift was smaller than for the pristine samples. Notice that again the behavior of the PtCo₆ catalyst deviates, which is not further discussed here. Concerning the observed shift in the de-alloyed samples the question arises, if such heavily de-alloyed NPs, which are not heat treated, exhibit a defined crystal structure. To our opinion referring to a single lattice parameter in such samples might be oversimplified. To obtain insight into their local structure, we characterized the material using PDF.

All PDFs (Fig. 7) reveal a high-intensity peak at $r \approx 2.75$ Å close to the expected Pt–Pt inter-atomic distance of 2.77 in bulk Pt²⁵ as well as peaks from more distant Pt–Pt pairs. No shoulders from Co–Pt at $r \approx 2.64$ Å or peak for Co–Co at $r \approx 2.50$ Å²⁵ are observed, in agreement with de-alloying, but also reflecting the low abundance and low scattering power of Co. The small peak at $r \approx 2.3$ Å, most pronounced for the pure Pt sample, most likely represents Pt(II)–Cl atomic pairs, which are expected to have a distance of 2.33 Å.³⁷ In EDS small amounts of Cl were detected as well, in the electrochemical measurements, Cl contamination was only evident in a few cases, where the effect could be removed by changing the electrolyte after initial cleaning of the samples.

At larger r -values in the PDF, the positions of peaks from more distant Pt–Pt pairs are shifted to slightly lower values for the Pt₃Co, PtCo and PtCo₃ samples (inset Fig. 7) and the size of the coherent scattering domains differ, with peaks extending to highest r -value for the pure Pt sample.

Using PDFgui, calculated PDFs were fitted to the experimental data. For catalysts with CTAB:total metal ratio of 3, Fig. 8 and Table 3 summarize the results for the size of the coherent scattering domains, the lattice constant parameters and the

atomic isotropic displacement parameters (U_{iso} ; depict thermal and static displacement of the atoms in the lattice), Table S1 (ESI†) summarizes the PDFgui results for all the nanoalloys.

Although the uncertainty of the fitting and the variation in the values obtained for materials from different synthesis is sizeable, we can identify certain trends. The average values suggest a decrease in the size of the coherent scattering domains and an increase in U_{iso} with increasing amount of Co in the initial material. Similar increase in U_{iso} has been observed for Pt–Au nanoparticles, reflecting increased disorder in the alloy compared to the pure end-members.³⁸ For the samples where the catalytic activity was measured (larger squares in Fig. 8), the fitted lattice constant parameters are decreased for samples with initial composition Pt₃Co, PtCo and PtCo₃. However, this trend is less obvious for the samples prepared with variable amount of CTAB. For PtCo₆, the lattice constant parameter is similar to the one of pure Pt, suggesting the structural collapse of such heavily de-alloyed samples. Notably, the U_{iso} shows some dependence on the size of the coherent scattering domains, consistent with findings from Shi *et al.*,³⁹ who interpreted the results to reflect increased thermal motion of surface atoms as well as an anomalous bond behavior for their smallest Pt sample (17.8 Å).

Working with PDFgui, fitted values may be interrelated. For example, U_{iso} , which portrays thermal and static displacement of atoms in the crystal lattice, as well as d_2 , which accounts for the correlated atomic movement in the sample, are fitted from peak widths, meaning that their values could be interdependent. The fitted values for d_2 are very alike for the Co containing samples (4.79 ± 0.13 Å²) with only the value for the pure Pt sample being noticeably different ($d_2 = 5.18$ Å²). Possibly, this discrepancy and the poorer goodness of fit (Rw; Table 3) relates to the presence of superimposed peaks from Cl and Pt(II) atomic pairs.

To probe peak positions and widths in more detail, the PDF peaks at various r -values were fitted with a Gaussian shape. The results indicate (i) that the peak positions for the Co-doped samples become increasingly offset from the position determined for Pt at higher r -values and (ii) that their peaks become broadened at r -values above 6 Å (Fig. S7, ESI†). This behavior is

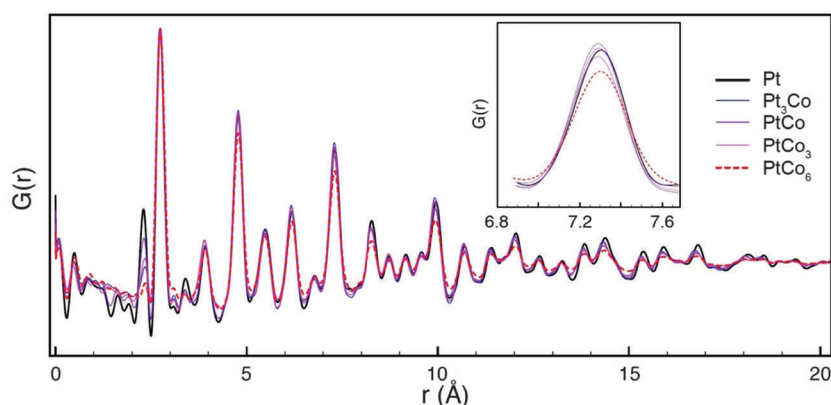


Fig. 7 PDF of pure Pt and de-alloyed CTAB synthesized Pt_xCo_{1-x} catalysts. Insert show details of peaks occurring at r -values between 5.8 and 7.6 Å.

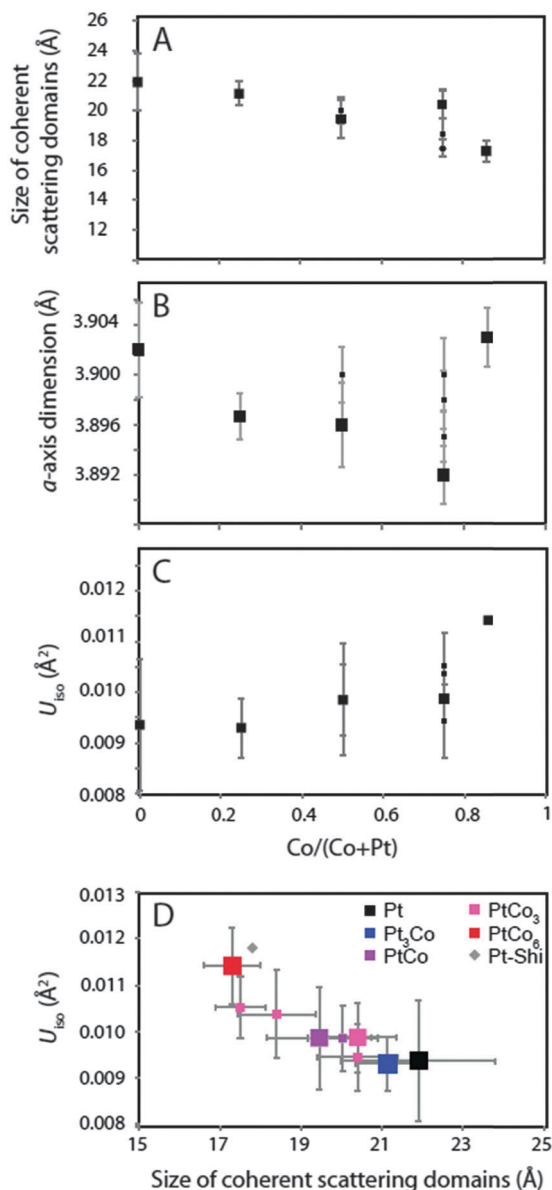


Fig. 8 Results of fitting with PDFgui. (A) The size of the coherent scattering domains, (B) the *a*-axis or lattice constant parameter and (C) the isotropic atomic displacement factor as a function of the relative amount of Co in the initial material. (D) The isotropic atomic displacement factor as a function of the fitted size of the coherent scattering domains. The large squares represent data measured for material, where catalytic activity was determined. Errors refer to one standard deviation. Measurements by Shi *et al.* are used as a reference.

similar to that observed for $\text{Ga}_{1-x}\text{In}_x\text{As}$ and $\text{ZnSe}_{1-x}\text{Te}_x$ alloys,^{40,41} where the introduction of a dopant results in significantly

increased displacement and broadening of peaks representing more distant neighbors as a result of bond bending to accommodate strain.

If the alloying element is poorly scattering and of low concentration, its presence does not result in a clear peak for the first neighbor, *e.g.*, no clear peak for Ga in $\text{In}_{0.83}\text{Ga}_{0.17}\text{As}$ in ref. 24, but peaks for more distant neighbors are nevertheless significantly displaced and broadened. Quite possibly, the presence of a very small amount of electron-lean Co in the material studied here, leads to similar appearance, although the Co effect on the peak width cannot readily be deconvoluted from the effect resulting from the size of coherent scattering domains. Assuming that the peak position for more distal neighbors follows Vegard's law, the displacement of peaks indicates a contraction of the unit cell to about 0.3% compared to the pure platinum Å, corresponding to a Co content of ~3.5% if its radius is set to 1.2485 Å,²⁵ in agreement with the low Co content after de-alloying, indicated by EDS.

The above analysis assumes that the material consists of structurally homogeneous nanoparticles. However, our data indicates that the $\text{Pt}_x\text{Co}_{1-x}$ catalysts might be composed of an 8 Å surface region composed largely of Pt and a core region containing Co.¹² This core-shell construction could give rise to two structurally distinct regions. No evidence of such structural inhomogeneity was found when fitting the PDF data with two components instead of simply one. Thus, it is not assumed that the materials should contain two components with distinctly different local order.

4. Conclusions

In this work, we investigated the effect of de-alloying on the structural and catalytic properties of colloidally prepared $\text{Pt}_x\text{Co}_{1-x}$ nanoalloys. In addition their stability was tested. The results indicate that the catalytic performance and stability of such de-alloyed catalysts increases with increasing initial Co content. However, there is a limit of how much material can be leached out before the structural integrity of the particles is affected and the catalysts become inactive and less stable. The common explanation for increased ORR activity in de-alloyed Pt alloys is surface strain. Both XRD and PDF suggests a decrease of the lattice constant parameter with moderate increase in Co content. PDF indicates that along with the strain, the surface disorder increases. However, the disorder of the PtCo_6 sample is highest, while strain and catalytic performance are decreased, which is interpreted by a structural collapse of the nanoparticles. Designing de-alloyed fuel cell catalysts one therefore needs to maximize disorder without inflicting a structural collapse of the active phase of the catalyst.

Table 3 Structural properties of CTAB synthesized, acid leached $\text{Pt}_x\text{Co}_{1-x}$ nanocatalysts obtained from PDF. The errors refer to the standard deviation (Rw)

Sample	Co/(Pt + Co)	Size of coherent scattering domains (Å)	d_2	Lattice constant CTAB (HCl) PDF (Å)	Lattice constant CTAB (HCl) XRD (Å)	U_{iso} (Å ²)
Pt	0.00	21.9 ± 1.9	5.2 ± 0.6	3.902 ± 0.004	—	0.0094 ± 0.0013
Pt ₃ Co	0.25	21.1 ± 0.8	4.7 ± 0.3	3.897 ± 0.002	3.903	0.0093 ± 0.0006
PtCo	0.50	19.5 ± 1.3	4.9 ± 0.5	3.896 ± 0.003	3.886	0.0099 ± 0.0011
PtCo ₃	0.75	20.4 ± 1.0	4.8 ± 0.4	3.892 ± 0.002	3.877	0.0099 ± 0.0008
PtCo ₆	0.86	17.3 ± 0.7	4.8 ± 0.3	3.903 ± 0.002	3.893	0.0114 ± 0.0008

Acknowledgements

This work was supported by the Danish DFF through grant# 10-081337 and the Carlsberg Foundation through an instrument grant. We acknowledge Andrea Mingers from the group of Dr Karl J. J. Mayrhofer at the MPIE Düsseldorf for the ICP-MS analysis. S.J. acknowledges funding from the European Commission in the framework of the MINSC ITN (Initial Training Research network), project number 290040. We are grateful for kind help given by Karina Chapman, Peter Chupas, Rick Spence and Kevin A. Beyer, APS beamline 11 ID-B. Use of the Advanced Photon Source was supported by the U. S. Department of Energy, Office of Science, Office of Basic Energy Sciences, under Contract No. DE-AC02-06CH11357.

References

- H. Y. Wolf Vielstich and A. Hubert, *Gasteiger Handbook of fuel cells: fundamentals, technology, and applications*, 2003.
- M. Lefèvre, E. Proietti, F. Jaouen and J.-P. Dodelet, *Science*, 2009, **324**, 71.
- V. Goellner, C. Baldizzone, A. Schuppert, M. T. Sougrati, K. Mayrhofer and F. Jaouen, *Phys. Chem. Chem. Phys.*, 2014, **16**, 18454.
- C.-J. Yang, *Energy Policy*, 2009, **37**, 1805.
- V. R. Stamenkovic, B. S. Mun, M. Arenz, K. J. J. Mayrhofer, C. A. Lucas, G. F. Wang, P. N. Ross and N. M. Markovic, *Nat. Mater.*, 2007, **6**, 241.
- H. A. Gasteiger, S. S. Kocha, B. Sompalli and F. T. Wagner, *Appl. Catal., B*, 2005, **56**, 9.
- J. Greeley, I. E. L. Stephens, A. S. Bondarenko, T. P. Johansson, H. A. Hansen, T. F. Jaramillo, J. Rossmeisl, I. Chorkendorff and J. K. Nørskov, *Nat. Chem.*, 2009, **1**, 552.
- A. S. Bandarenka, A. S. Varela, M. Karamad, F. Calle-Vallejo, L. Bech, F. J. Perez-Alonso, J. Rossmeisl, I. E. Stephens and I. Chorkendorff, *Angew. Chem., Int. Ed.*, 2012, **51**, 11642.
- K. J. J. Mayrhofer, K. Hartl, V. Juhart and M. Arenz, *J. Am. Chem. Soc.*, 2009, **131**, 16348.
- H. Haas and M. Davis, *ECS Trans.*, 2009, **25**, 1623.
- P. Mani, R. Srivastava and P. Strasser, *J. Power Sources*, 2011, **196**, 666.
- M. Oezaslan, M. Heggen and P. Strasser, *J. Am. Chem. Soc.*, 2012, **134**, 514.
- F. Hasché, M. Oezaslan and P. Strasser, *J. Electrochem. Soc.*, 2011, **159**, B24.
- C. Wang, M. Chi, D. Li, D. van der Vliet, G. Wang, Q. Lin, J. F. Mitchell, K. L. More, N. M. Markovic and V. R. Stamenkovic, *ACS Catal.*, 2011, **1**, 1355.
- D. Li, C. Wang, D. Tripkovic, S. Sun, N. M. Markovic and V. R. Stamenkovic, *ACS Catal.*, 2012, **2**, 1358.
- Y. Wang, J. Ren, K. Deng, L. Gui and Y. Tang, *Chem. Mater.*, 2000, **12**, 1622.
- J. Speder, L. Altmann, M. Roefzaad, M. Baumer, J. J. K. Kirkensgaard, K. Mortensen and M. Arenz, *Phys. Chem. Chem. Phys.*, 2013, **15**, 3602.
- J. Speder, L. Altmann, M. Bäumer, J. J. Kirkensgaard, K. Mortensen and M. Arenz, *RSC Adv.*, 2014, **4**, 14971.
- P. Strasser, S. Koh, T. Anniyev, J. Greeley, K. More, C. F. Yu, Z. C. Liu, S. Kaya, D. Nordlund, H. Ogasawara, M. F. Toney and A. Nilsson, *Nat. Chem.*, 2010, **2**, 454.
- A. P. Hammersley, S. O. Svensson and A. Thompson, *Nucl. Instrum. Methods Phys. Res., Sect. A*, 1994, **346**, 312.
- A. P. Hammersley, *FT2D: An introduction and overview*, ESRF Internal Report ESRF97HA02T, 1997.
- P. J. Chupas, X. Y. Qiu, J. C. Hanson, P. L. Lee, C. P. Grey and S. J. L. Billinge, *J. Appl. Crystallogr.*, 2003, **36**, 1342.
- X. Qiu, J. W. Thompson and S. J. L. Billinge, *J. Appl. Crystallogr.*, 2004, **37**, 678.
- C. L. Farrow, P. Juhas, J. W. Liu, D. Bryndin, E. S. Bozin, J. Bloch, T. Proffen and S. J. L. Billinge, *J. Phys.: Condens. Matter*, 2007, **19**, 335219.
- R. W. G. Wyckoff, *Crystal Structures*, 1963, vol. 1.
- K. J. J. Mayrhofer, G. K. H. Wiberg and M. Arenz, *J. Electrochem. Soc.*, 2008, **155**, P1.
- M. Nesselberger, S. Ashton, J. C. Meier, I. Katsounaros, K. J. J. Mayrhofer and M. Arenz, *J. Am. Chem. Soc.*, 2011, **133**, 17428.
- S. Wang, L. Kuai, Y. Huang, X. Yu, Y. Liu, W. Li, L. Chen and B. Geng, *Chem. – Eur. J.*, 2013, **19**, 240.
- L. Biao, G. Jian-guo, W. Qi and Z. Qing-jie, *Mater. Trans.*, 2005, **46**, 1865.
- S. S. Kalyan Kamal, P. K. Sahoo, M. Premkumar, N. V. Rama Rao, T. Jagadeesh Kumar, B. Sreedhar, A. K. Singh, S. Ram and K. Chandra Sekhar, *J. Alloys Compd.*, 2009, **474**, 214.
- M. Marlene González, P. Santiago-Jacinto, P. Santiago-Jacinto, E. Reguera and R.-G. Geonel, *Nano-Micro Lett.*, 2011, **3**, 12.
- I. Spanos, J. J. K. Kirkensgaard, K. Mortensen and M. Arenz, *J. Power Sources*, 2014, **245**, 908.
- M. Hayes and A. T. Kuhn, *Appl. Surf. Sci.*, 1980, **6**, 1.
- T. Biegler, D. A. J. Rand and R. Woods, *J. Electroanal. Chem. Interfacial Electrochem.*, 1971, **29**, 269.
- J. Clavilier, D. Armand, S. G. Sun and M. Petit, *J. Electroanal. Chem. Interfacial Electrochem.*, 1986, **205**, 267.
- A. Zana, J. Speder, M. Roefzaad, L. Altmann, M. Bäumer and M. Arenz, *J. Electrochem. Soc.*, 2013, **160**, F608.
- F. R. Hartley, *Nature, Phys. Sci.*, 1972, **236**, 75.
- V. Petkov, S. Shastri, B. Wanjala, R. Loukrakpam, J. Luo and C. J. Zhong, *Z. Kristallogr. - Cryst. Mater.*, 2012, **227**, 262.
- C. Y. Shi, E. L. Redmond, A. Mazaheripour, P. Juhas, T. F. Fuller and S. J. L. Billinge, *J. Phys. Chem. C*, 2013, **117**, 7226.
- V. Petkov, I. K. Jeong, J. S. Chung, M. F. Thorpe, S. Kycia and S. J. L. Billinge, *Phys. Rev. Lett.*, 1999, **83**, 4089.
- P. Peterson, T. Proffen, I. K. Jeong, S. Billinge, K. S. Choi, M. Kanatzidis and P. Radaelli, *Phys. Rev. B: Condens. Matter Mater. Phys.*, 2001, **63**, 165211.